

# Continuum Robot State Estimation with Actuation Uncertainty

James M. Ferguson<sup>1</sup>, Alan Kuntz<sup>2</sup>, and Tucker Hermans<sup>1,3</sup>

**Abstract**—Continuum robots are flexible, thin manipulators capable of navigating confined or delicate environments making them well suited for surgical applications. Previous approaches to continuum robot state estimation typically rely on simplified, deterministic actuation models. In contrast, our method jointly estimates robot shape, external loads, internal stresses, and actuation inputs. We adopt a discrete Cosserat rod formulation and show that, when paired with a midpoint integration rule, it achieves high numerical accuracy with relatively few state nodes. This discretization naturally induces a factor-graph structure for sparse nonlinear optimization on  $SE(3)$ . We extend the formulation with actuation factors for tendon-driven robots and combine multiple rod graphs for parallel continuum robots with closed-loop topologies. By explicitly including actuation variables in the state, the linearized system can be reused to extract manipulator Jacobians, which we leverage in performing trajectory tracking. Finally, we validate the approach experimentally on a surgical concentric tube robot. Overall, our approach enables principled, real-time estimation across multiple continuum robot architectures, accounting for actuation uncertainty and providing direct access to manipulator Jacobians.

## I. INTRODUCTION

Continuum robots are thin, tentacle-like manipulators whose backbones deform continuously in response to actuation and external loading. Their compliance and slender geometry make them particularly well suited for medical/surgical applications [1]. The primary objective of continuum robot modeling is to predict backbone shape under actuation, which is classically formulated as a deterministic Boundary Value Problem (BVP) in arlength, where the Cosserat rod equations act as hard dynamic constraints [2].

Beyond shape prediction, an important objective is to quantify uncertainty in backbone configurations or to improve accuracy using external observations. Even accurate models are affected by unmodeled effects, parameter uncertainty, and actuator variability. This motivates state estimation approaches [3], [4] that have been adapted from temporal dynamics to the continuum robot arlength domain [5]–[9]. However, these prior works either do not model actuation explicitly or treat actuator inputs deterministically using simplified models.

In this letter, we extend these approaches by incorporating probabilistic, mechanically principled actuation models. We

Research reported in this publication was supported by the Advanced Research Projects Agency for Health (ARPA-H) under the ALISS project, Award Number D24AC00415-00. The ARPA-H award of up to \$11,935,038 provided 100% of the financial support for this work. The opinions and findings in this paper is solely the responsibility of the authors and do not necessarily represent the official views of ARPA-H.

<sup>1</sup>The Kahlert School of Computing and Robotics Center, University of Utah, USA. <sup>2</sup>Department of Electrical and Computer Engineering and Department of Computer Science, Vanderbilt University, TN, USA. <sup>3</sup>NVIDIA, Seattle, WA, USA. Correspondence: j.m.ferguson@utah.edu

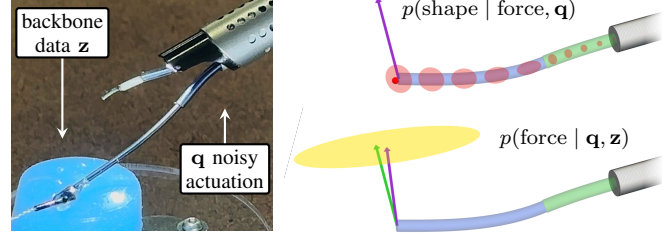


**Fig. 1:** *Left:* Our approach fuses uncertain actuation inputs and external backbone measurements with a prior mechanics model. *Right:* Example snapshot results from our experiments. When interaction forces are known (or assumed zero), we estimate a distribution for robot shape (top). In the more realistic case where loads are unknown, our approach estimates a conditional distribution for external loading, given backbone observations (bottom).

introduce a discrete arlength factor-graph representation of the Cosserat rod model and demonstrate that a midpoint strain rule achieves high numerical accuracy while requiring relatively few backbone variables. Building on this formulation, we derive a probabilistic coupled tendon actuation model and additionally show how multiple Cosserat rod graphs can be combined for parallel continuum robot estimation. These extensions are evaluated in simulation by comparing open-loop solutions to standard BVP benchmarks. By explicitly representing actuation variables within the graph, the resulting joint marginals naturally enable extraction of manipulator Jacobians, which we validate in simulation. Finally, we demonstrate the approach experimentally on a surgical concentric tube robot. Our results demonstrate a principled, real-time framework (open-source upon acceptance) for continuum robot estimation across diverse actuation models, providing direct access to manipulator Jacobians for downstream use.

## II. RELATED WORK

Many approaches to continuum robot state estimation have operated without explicitly incorporating a prior mechanics model. Early work used geometric curve fitting from external sensors [10]–[12] or Fiber Bragg Grating (FBG) arrays [13], [14] to reconstruct backbone shape, often via dead-reckoning. While simple and effective, these methods forgo prior mechanical knowledge that could improve accuracy with limited observations. Learning-based methods regress backbone shape from data using neural networks [15], [16], achieving high accuracy in trained regimes but requiring retraining for new actuation or sensing configurations.

To leverage prior mechanics, several groups fit deterministic BVP models to observed data. Black et al. estimated tip forces in parallel robots [17], and Aloï et al. optimized

distributed external loads in tendon-driven robots [18]. These approaches, however, typically lack a principled treatment of uncertainty, which is critical given the ill-conditioned inverse problems of continuum robots [6], [18], [19].

Probabilistic treatments address this limitation. Rucker et al. inferred distributions over tip forces [19], and Kalman-based methods have been applied to continuum robot guidance and force sensing [20]–[22]. Anderson et al. first modeled Cosserat rods as a stochastic process for parallel configurations [5]. Lilge et al. [7], [8] framed continuum robot state estimation as Gaussian process regression with a Cosserat rod prior, enabling principled fusion of model and measurement information. This framework was later extended to incorporate actuation inputs [9] by modifying the prior mean with a deterministic point-moment tendon actuation model. While this extension improved estimation accuracy, the point-moment approximation neglects force–shape coupling effects and is known to be less accurate than fully coupled formulations, particularly under external loading conditions [23]. Ferguson et al. [6] proposed joint shape and load estimation, demonstrating a single tendon robot example, but their actuation model was deterministic and not linearized for optimization.

In contrast, our approach explicitly couples force and shape and represents actuation variables directly within the estimation graph. We demonstrate real-time estimation across three major classes of continuum robots—(i) tendon-driven, (ii) parallel continuum, and (iii) concentric tube—unlike [6], which focused on simple rods and did not achieve real-time performance.

Collocation and weighted-residual methods [24]–[27] are conceptually related, but typically not probabilistic. Sparse nonlinear optimization, by contrast, has been highly effective for robotic estimation and control, including SLAM [4], forward/inverse dynamics [28], constrained trajectory optimization [29], [30], and motion planning [31].

### III. COSSERAT ROD MODEL

To model continuum robot backbones, we adopt the Cosserat rod model formalized for state estimation by Lilge et al. [7]. We use the conventions that pose  $\mathbf{T} = \{R, t\} \in \text{SE}(3)$  maps body to spatial coordinates and Lie algebra elements  $\varepsilon = (\omega, \nu) \in \mathfrak{se}(3)$  are represented with their rotational components first imposing the adjoint representations

$$\text{Ad}(\mathbf{T}) = \begin{bmatrix} R & 0 \\ t^\wedge R & R \end{bmatrix} \quad \text{ad}_\varepsilon = \begin{bmatrix} \omega^\wedge & 0 \\ \nu^\wedge & \omega^\wedge \end{bmatrix}. \quad (1)$$

where  $\varepsilon^\wedge = [\omega^\wedge \ \nu; 0 \ 0]$ , and the hat operator  $(\cdot)^\wedge$  maps  $\mathbb{R}^3$  to skew-symmetric matrices (i.e.  $\omega^\wedge v = \omega \times v$ ).

The Cosserat kinematic equation prescribe that pose evolves in arclength according to

$$\frac{d}{ds} \mathbf{T}(s) = \mathbf{T}(s) \varepsilon(s)^\wedge, \quad \varepsilon(s) = \begin{bmatrix} \omega(s) \\ \nu(s) \end{bmatrix}, \quad (2)$$

where  $\omega(s)$  and  $\nu(s)$  are the angular and linear spatial rates. The (body frame) generalized strain  $\varepsilon(s) \in \mathbb{R}^6$  deviates from

its nominal, stress-free value  $\bar{\varepsilon}(s)$  under loading based on the material constitutive law

$$\boldsymbol{\sigma}(s) = \begin{bmatrix} \mathbf{m}(s) \\ \mathbf{n}(s) \end{bmatrix} = \mathcal{K} (\varepsilon(s) - \bar{\varepsilon}(s)), \quad (3)$$

which relates the generalized stress  $\boldsymbol{\sigma}(s)$ —comprising internal moment  $\mathbf{m}(s)$  and force  $\mathbf{n}(s)$ —to the strain through the stiffness matrix  $\mathcal{K}$ , which encodes sensitivity to shear, elongation, bending, and torsion.

Lilge et al. [7] highlighted the similarity of the Cosserat rod model to classical rigid body dynamics, with the following differential relationship between stress, strain, and the external distributed wrench  $\mathbf{f}(s) \in \mathbb{R}^6$  along the rod. Rewriting in our frame convention, stress propagates through the rod based on

$$\frac{d}{ds} \boldsymbol{\sigma}(s) = \text{ad}_{\varepsilon(s)}^T \boldsymbol{\sigma}(s) - \mathbf{f}(s). \quad (4)$$

Direct stochastic integration of (4) is complicated by the coupling of internal stress variables with shape through the  $\text{SE}(3)$  integration (2).

#### A. Discrete Kinematics Noise Model

In an effort to handle the stress–shape coupling described above, we deviate from the continuous arclength formulation [6]–[8], [32] by discretizing the arclength domain and using a midpoint strain integration rule to ensure good integration accuracy. Our representation is conceptually related to deterministic discrete Cosserat formulations such as [33].

The discrete version of the kinematics (2) is identical to rigid body kinematics [3]. Assuming that strain  $\varepsilon_k = \varepsilon(s_k)$  is constant over the interval  $[s_k, s_{k+1}]$  and  $\Delta s = s_{k+1} - s_k$  is spatially uniform, the discrete version of (2) is

$$\mathbf{T}_{k+1} = \mathbf{T}_k \exp(\Delta s \varepsilon_k^\wedge). \quad (5)$$

Note that we write all unknown variables to be estimated in bold, roman, uppercase type (e.g.  $\mathbf{T}_k = \mathbf{T}(s_k)$ ).

Now by rearranging (3) and adding Gaussian noise, the generalized strain  $\varepsilon_k$  is related to stress  $\mathbf{S}_k = \boldsymbol{\sigma}(s_k)$  by

$$\varepsilon_k = \mathcal{K}^{-1} \mathbf{S}_k + \bar{\varepsilon}_k + \mathbf{n}_{T_k}, \quad \mathbf{n}_{T_k} \sim \mathcal{N}(0, \Sigma_T), \quad (6)$$

where  $\bar{\varepsilon}_k$  encodes the nominal shape of the rod in its unstressed state. Thus,  $\mathbf{n}_{T_k}$  models uncertainty in the initial shape of the rod, as well as any deviations from linear elasticity. The above is akin to an Euler integration method, but we found that significant shape accuracy gains can be had by instead using a midpoint strain rule:

$$\varepsilon_k = \frac{1}{2} \mathcal{K}^{-1} (\mathbf{S}_k + \mathbf{S}_{k+1}) + \bar{\varepsilon} + \mathbf{n}_{\varepsilon_k}, \quad (7)$$

where strain over the interval is computed based on the average of  $\mathbf{S}_k$  and  $\mathbf{S}_{k+1}$ . Combining with (5), we define our full kinematics error model

$$\mathbf{e}_{T_k} = \Delta s \left( \frac{1}{2} \mathcal{K}^{-1} (\mathbf{S}_k + \mathbf{S}_{k+1}) + \bar{\varepsilon} \right) - \ln (\mathbf{T}_k^{-1} \mathbf{T}_{k+1})^\vee, \quad (8)$$

which imposes a likelihood factor  $J_{T_k} = \|\mathbf{e}_{T_k}\|_{\Sigma_T}$ , penalizing shape deviations from elasticity theory. See Appendix I for error model linearizations.

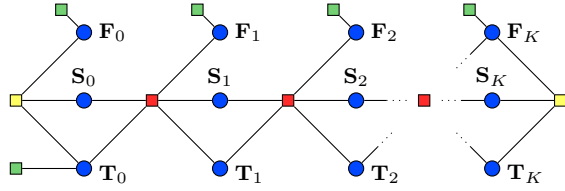


**Fig. 2:** Factor graph representation of the discrete Cosserat rod model, the core graph module in our robots. Internal factors (red) encode noisy Cosserat equation constraints between state variables. To make the problem well-posed, appropriate boundary conditions (e.g. fixed base pose and known wrenches) must be specified as prior factors (green). Boundary factors (yellow) enforce consistency between the tip wrenches and tip stresses.

### B. Discrete Mechanics Noise Model

To discretize the mechanics (4), we approximate the loading as discrete forces applied at the  $K$  node locations. This approximation is exact when loads are inherently discrete (e.g., a finite number of tendon routing discs). For truly distributed loads, a sufficiently fine discretization can be used, allowing for accurate approximation. Given discrete wrenches, we rewrite the (4) in the spatial frame  $(\cdot)^w$ :

$$\frac{d}{ds} \boldsymbol{\sigma}^w(s) = -\mathbf{f}^w(s) = -\sum_{k=1}^K \delta(s - s_k) \mathbf{F}_k^w. \quad (9)$$

Since  $\frac{d}{ds} \boldsymbol{\sigma}^w(s) = 0$  on the interior, we evaluate directly on the endpoints and add the point wrench at  $k + 1$ :

$$\boldsymbol{\sigma}^w(s_{k+1}) = \boldsymbol{\sigma}^w(s_k) - \mathbf{F}_{k+1}^w \quad (10)$$

Rewriting back in the body frame, manipulating, and allowing for Gaussian noise,

$$\mathbf{S}_{k+1} = \text{Ad}^T(\mathbf{T}_k^{-1} \mathbf{T}_{k+1}) \mathbf{S}_k - \text{Rot}^T(\mathbf{T}_{k+1}) \mathbf{F}_{k+1}^w + \mathbf{n}_{S_k}, \quad (11)$$

where  $\text{Ad}^T(\cdot)$ , transports a wrench seen in frame  $K$  to frame  $K + 1$ . The operator  $\text{Rot}(\cdot)$  is used to transform wrench coordinates between spatial and body frames; i.e.,  $\text{Rot}(\mathbf{T}_k) = [R_k \ 0; 0 \ R_k]$ .

We drop the frame notation  $(\cdot)^w$  and adopt the convention that wrenches are estimated in the world frame. Rearranging, we arrive at

$$\mathbf{e}_{S_k} = \text{Ad}^T(\mathbf{T}_k^{-1} \mathbf{T}_{k+1}) \mathbf{S}_k - \text{Rot}^T(\mathbf{T}_{k+1}) \mathbf{F}_{k+1} - \mathbf{S}_{k+1}, \quad (12)$$

with associated likelihood  $J_{S_k} = \|\mathbf{e}_{S_k}\|_{\Sigma_S}$ , which penalizes deviations from ideal stress propagation through the rod. In practice, we set the noise level  $\mathbf{n}_{S_k} \sim \mathcal{N}(0, \Sigma_S)$  to a small value to softly enforce equality.

### C. Boundary Values and Prior Factors

At the base and tip of the rod, the stresses must be caused solely by the associated base and tip wrenches. The following noise model enforces this constraint:

$$\mathbf{e}_{B_0} = \mathbf{S}_0 + \text{Rot}^T(\mathbf{T}_0) \mathbf{F}_0, \quad \mathbf{e}_{B_K} = \mathbf{S}_K - \text{Rot}^T(\mathbf{T}_K) \mathbf{F}_K, \quad (13)$$

with associated likelihoods  $J_{B_0} = \|\mathbf{e}_{B_0}\|_{\Sigma_B}$  and  $J_{B_K} = \|\mathbf{e}_{B_K}\|_{\Sigma_B}$ . We additionally anchor the base pose in the

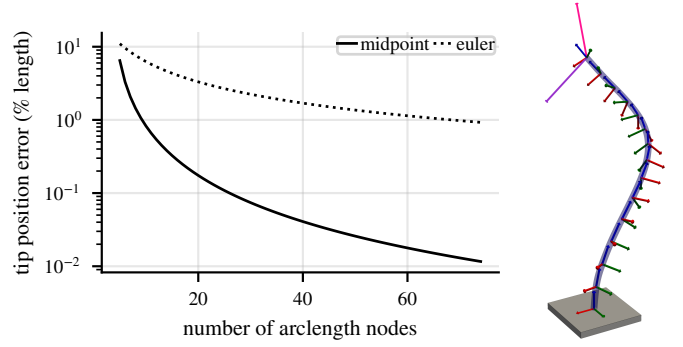


**Fig. 3:** *Left:* Average numerical integration tip position accuracy of our discrete Cosserat rod model, compared to a boundary value ODE solver benchmark. Error is sharply attenuated as the number of discretization nodes increases when using our midpoint strain rule. *Right:* Example evaluation configuration. We evaluate over 540 different tip wrenches comprising force (violet) and moment (magenta) vectors.

spatial frame using the prior factor

$$J_0 = \|\mathbf{e}_0\|_{\Sigma_0}, \quad \mathbf{e}_0 = \ln(\bar{\mathbf{T}}_0^{-1} \mathbf{T}_0)^\vee, \quad (14)$$

which penalizes deviations of  $\mathbf{T}_0$  from its prior mean  $\bar{\mathbf{T}}_0$ .

To solve the system, additional factors need to be placed on the wrench variables  $\mathbf{F}_k$ . To model a Cosserat rod under known loading conditions, this can be done by attaching prior factors:

$$J_{F_k} = \|\mathbf{e}_{F_k}\|_{\Sigma_{F_k}}, \quad \mathbf{e}_{F_k} = \mathbf{F}_k - \bar{\mathbf{F}}_k. \quad (15)$$

In Section IV, we show how to instead attach actuation factors for more realistic scenarios.

### D. Sparse Nonlinear Optimization

Given the error models, we show how to solve the base Cosserat rod model using our framework, writing out the explicit likelihood equations for Maximum A Posteriori (MAP) estimation. Given the Cosserat rod error models, the full negative log probability is proportional to a quadratic likelihood given by

$$J(\mathbf{T}_{0:K}, \mathbf{S}_{0:K}, \mathbf{F}_{0:K}) = J_{B_0} + J_{B_K} + J_0 + \sum_{k=0}^{K-1} (J_{T_k} + J_{S_k}) + \sum_{k=1}^K J_{F_k}. \quad (16)$$

Figure 2 gives the corresponding factor graph representation. In the case of Gaussian noise, (16) defines a sparse nonlinear least squares problem.

We implement the graph in GTSAM using the linearizations in Appendix I, solving with a dogleg optimizer and taking the Laplace approximation at the MAP solution as the posterior. Since we iterate to completion at each time step, we additionally warm start using the previous solution, whenever available. After solution, GTSAM enables efficient extraction of marginal/joint covariances between arbitrary sets of variables [4]. In the case of pose variables, marginals are represented as mean  $\bar{\mathbf{T}}_k \in SE(3)$  perturbed by the random twist  $\boldsymbol{\xi}_k$  in the local tangent space:

$$\mathbf{T}_k = \bar{\mathbf{T}}_k \exp(\hat{\boldsymbol{\xi}}_k), \quad \boldsymbol{\xi}_k \sim \mathcal{N}(0, \Sigma_{T_k T_k}). \quad (17)$$

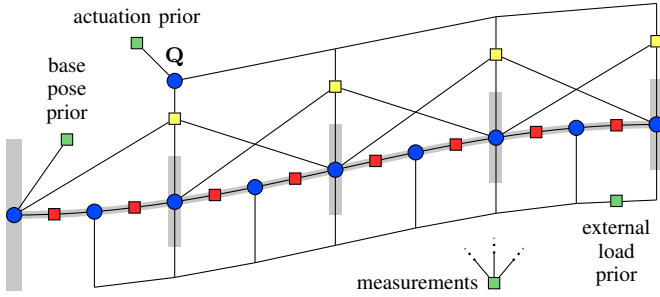


**Fig. 4:** Factor graph representation of the discrete Cosserat rod model with tendon actuation (showing one node between each disc and only 4 discs for clarity). The nodes and factors (red) along the rod are a condensed version of the Cosserat rod graph (see Figure 2). The tendon actuation factors (yellow) model the transmission of tension into backbone wrenches. Given prior actuation and external loads, the graph models forward kinematics with uncertainty. The inverse problem—estimating external loads—is solved by attaching measurement factors to backbone states.

### E. Simple Cosserat Rod Simulations

To determine how many discretization nodes  $K$  are required for good numerical accuracy, we performed a simulation where we solved a Cosserat many times while varying the tip wrench (see Figure 3). The results are compared to a baseline BVP solver to compute any errors in numerical integration.

We see that the midpoint noise model (7) achieves 1% error with only  $K = 10$  nodes and 0.1% with less than  $K = 30$ , while the Euler noise model (6) did not achieve good accuracy in our study. This demonstrates that a discrete Cosserat formulation, which we find more practical for modeling actuation, is accurate and requires relatively few state variables.

## IV. TENDON-DRIVEN CONTINUUM ROBOTS

In general, a priori knowledge of the applied loads  $\mathbf{F}_k$  is not directly available. Instead, we must relate measured actuator values (e.g. tendon tensions) to the  $\mathbf{F}_k$  via an actuation model. Here we consider the actuation  $\mathbf{Q} \in \mathbb{R}^N$  as a random variable with a simple prior factor induced by the measured values  $\mathbf{q}$ :

$$\|\mathbf{Q} - \mathbf{q}\|_{\Sigma_Q}. \quad (18)$$

In the remainder of this section, we extend the base Cosserat rod graph to include tendon actuation by connecting  $\mathbf{Q}$  to the wrenches  $\mathbf{F}_k$  through actuation factors (see Figure 4). The physics is based on [34], which we extend for state estimation.

We assume that the tendon routing discs are coincident with a subset of the arclength nodes:  $\mathcal{D} = \{d_0, d_1, \dots, d\} \subseteq \{0, 1, \dots, K\}$ . We model the general case where each node, including disc nodes, may include an external wrench  $\mathbf{E}_k$ . For nodes which are not at discs ( $k \notin \mathcal{D}$ ), we simply set  $\mathbf{F}_k = \mathbf{E}_k$ .

For nodes that are at discs ( $k = d \in \mathcal{D}$ ), we sum

contributions from  $\mathbf{E}_k$  and from tendon actuation:

$$\mathbf{F}_d = \sum_{i=1}^N \left( \mathbf{f}_{d,i}^{d-1} + \mathbf{f}_{d,i}^{d+1} \right) + \mathbf{E}_d + \mathbf{n}_{D_d}. \quad (19)$$

The wrenches  $\mathbf{f}_{d,i}^{d-1}$  and  $\mathbf{f}_{d,i}^{d+1}$  are due to the tensile force from tendon  $i$  in the direction of the previous and next discs acting on disc  $d \in \mathcal{D}$ . The noise  $\mathbf{n}_{D_d} \sim \mathcal{N}(0, \Sigma_{D_d})$  models small deviations such as tendon-disc friction.

The single wrenches  $\mathbf{f}_{d,i}^j$ , due to the previous or next disc ( $j = \{d-1, d+1\}$ ) are computed based on the  $i^{\text{th}}$  tension  $q_i$  and the relative routing disc hole locations:

$$\begin{aligned} \mathbf{f}_{d,i}^j &= \text{Rot}(\mathbf{T}_d) \begin{bmatrix} \mathbf{h}_{d,i}^j \\ \mathbf{I} \end{bmatrix} \tilde{\mathbf{f}}_{d,i}^j, & \tilde{\mathbf{f}}_{d,i}^j &= q_i \frac{\mathbf{d}_{d,i}^j}{\|\mathbf{d}_{d,i}^j\|}, \\ \mathbf{d}_{d,i}^j &= [\mathbf{I}_{3 \times 3} \quad 0] \mathbf{T}_d^{-1} \mathbf{T}_j \begin{bmatrix} \mathbf{h}_{j,i} \\ 1 \end{bmatrix} - \mathbf{h}_{d,i}. \end{aligned} \quad (20)$$

Here the normalized difference in (body frame) hole locations  $\mathbf{h}_{d,i}$ ,  $\mathbf{h}_{j,i}$  is taken as the direction of the tendon force, scaled by  $q_i$ . Overall, we rearrange (20), to form an error model:

$$\mathbf{e}_{D_d} = \sum_{i=1}^N \left( \mathbf{f}_{d,i}^{d-1} + \mathbf{f}_{d,i}^{d+1} \right) + \mathbf{E}_d - \mathbf{F}_d, \quad (21)$$

with associated likelihood  $J_{D_d} = \|\mathbf{e}_{D_d}\|_{\Sigma_{D_d}}$ . This corresponds to the yellow factors in Figure 4, linking tension variables to backbone wrenches.

The graph is optimized in the same way as in Section III-D and can be run in different operating modes depending on the chosen external wrench  $\mathbf{E}_k$  priors. The  $\mathbf{E}_k$  are usually unknown, so their means are set to zero (except during ground truth simulation). Their covariances encodes prior belief: small when you assume no external load at  $k$  and large when you want to infer the force at that location. Figure 5 shows simulation examples in three distinct use cases. Additional information is required to close the loop when estimating  $\mathbf{E}_k$ . For this we use simple tip position measurements that are common in deflection-based force sensing [19]:

$$\mathbf{z}_p = \text{Pos}(\mathbf{T}_K) + \mathbf{n}_p, \quad \mathbf{n}_p \sim \mathcal{N}(\mathbf{0}, \Sigma_p). \quad (22)$$

### A. Manipulator Jacobian Extraction

Given the current state, we would additionally like to move the robot to a desired configuration, which can be accomplished using the manipulator Jacobian  $J_{T_K Q}$  relating actuation variables to tip motion. Instead of using finite differences [17] or a separate sensitivity ODE integration [35], we show how to extract  $J_{T_K Q}$  immediately from our solution.

Given the linearized graph after iteration, we immediately have access to the joint covariance  $\Sigma_{T_K Q}$  between  $\mathbf{T}_K$  and  $\mathbf{Q}$ , as well as the marginal covariance  $\Sigma_{QQ}$  so that the best linear predictor of  $\boldsymbol{\xi}_k$  given  $\mathbf{Q}$  is

$$\begin{aligned} \mathbb{E}(\boldsymbol{\xi}_K | \mathbf{Q}) &\approx \Sigma_{T_K Q} \Sigma_{QQ}^{-1} (\mathbf{Q} - \bar{\mathbf{Q}}) = J_{T_K Q} \delta \mathbf{Q}, \\ &\implies J_{T_K Q} = \Sigma_{T_K Q} \Sigma_{QQ}^{-1}, \end{aligned} \quad (23)$$

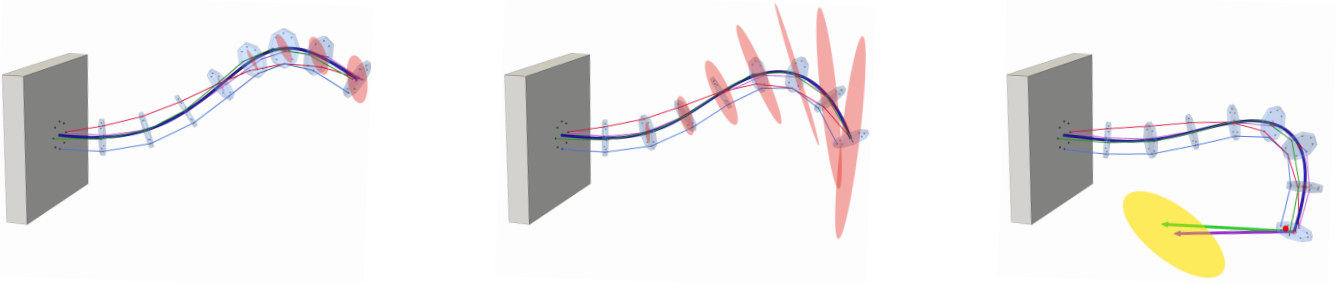


**Fig. 5:** Example snapshots from our tendon robot simulations illustrating different operating modes. *Left:* Forward kinematics with actuation/modeling uncertainty (i.e. no external wrenches). The red ellipses illustrate the position components of pose uncertainty ( $2 - \sigma$ ) along the backbone, subsampled at the disc locations. *Middle:* Prior distribution, given an unknown (zero mean with high prior uncertainty) tip force. *Right:* Posterior tip force distribution, given a noisy tip position measurement (red point). The violet and green arrows indicate the MAP estimate and ground truth forces with force uncertainty (gold). Additionally, the robot tracks the red point throughout our simulation, in spite of the uncertain tip force.

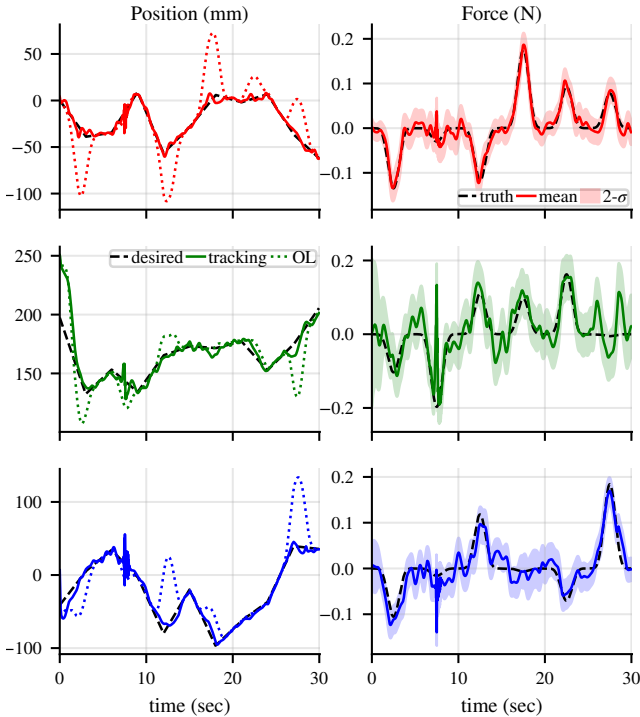


**Fig. 6:** Tendon robot simulation results (18.37 ms mean solve time over 900 time steps). Note red, green, and blue indicate  $x$ ,  $y$ , and  $z$  components throughout. *Left:* Position tracking in the presence of unknown loads. For comparison, we additionally show an open-loop (OL) trajectory, without position feedback. *Right:* Estimated tip forces while tracking. The shaded regions show  $2 - \sigma$  uncertainty envelopes, and the dotted lines indicate ground truth.

where we note that by definition of  $\xi_K$ , the Jacobian is in body frame coordinates.

Extraction of  $J_{T_K Q}$  from the marginals provides a convenient way to reuse the graph linearization to get the Jacobian. We demonstrate the use of  $J_{T_K Q}$  for trajectory following in our numerical experiments with both tendon-driven and parallel robots.

### B. Numerical Integration Benchmark Comparison

We compare our MAP solution with a deterministic BVP solver based on [34] to test numerical integration accuracy without any backbone observations. First, we use

the marginal-based Jacobian (23) to generate an open-loop actuation trajectory moving the tip position through a set of waypoints with zero loading. We separately generate a time-varying tip force whose magnitude pulses smoothly and direction changes continuously. Given ground truth actuation and tip force, we solved for the MAP estimate at each time step using our approach (Figure 6, left). We also solve with the BVP benchmark and compared the output with our method.

This resulted in an average numerical integration tip position error of 1.3% robot length over the trajectory when comparing with the deterministic baseline. Given the relatively coarse discretization ( $K = 30$  nodes, midpoint), this result shows that our overall tendon robot model is accurate compared to a BVP benchmark, without any backbone observations (i.e. forward mechanics).

### C. Position Tracking with Tip Force Estimation

In the previous section, unknown tip forces pushed the tip away from the desired trajectory. Here we add external backbone observations to estimate the forces and ultimately reject such disturbances. To estimate the tip force, we use noisy tip position and actuation measurements gathered from a separate ground truth model. Given the measurement factors, we estimate the full state, including tip force online (see Figure 5, right). We use a damped velocity control law using the marginal-based Jacobian (23) to update the commanded tendon tensions for closed loop position tracking, given the estimated force. Tracking and estimation results are detailed in Fig. 6.

Compared to the open-loop model, our approach was able to track position over the trajectory, and the force sensing results show good estimates of tip force. Estimation was fast (18 ms), compared to [6] (4000 ms), highlighting the efficiency of the sparse optimization. Early in the trajectory, the robot encountered an unstable force/shape configuration (jagged lines). In future work it may be possible to use the factor graph structure to detect and avoid such unstable configurations online. Overall these results show the feasibility of tendon robot shape/force estimation and trajectory tracking using the marginal-based Jacobian (23).

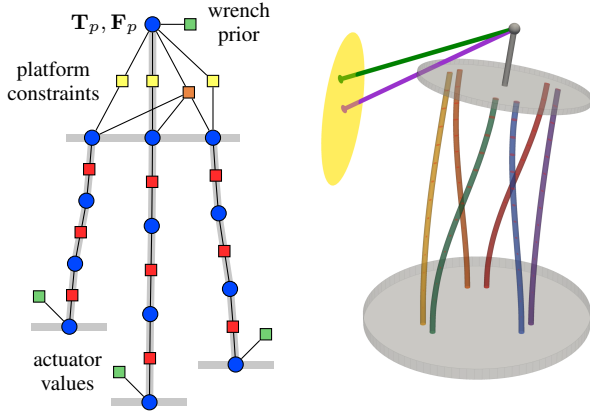


**Fig. 7:** *Left:* Factor graph representation of a parallel robot with base actuation [17]. Multiple Cosserat graphs (see Figure 2) are connected to a shared platform constraining relative poses (yellow) and tip wrenches (orange). Priors from measured actuator positions/efforts constrain rod base states (green). *Right:* Example estimation including external force, given the actuator measurements.

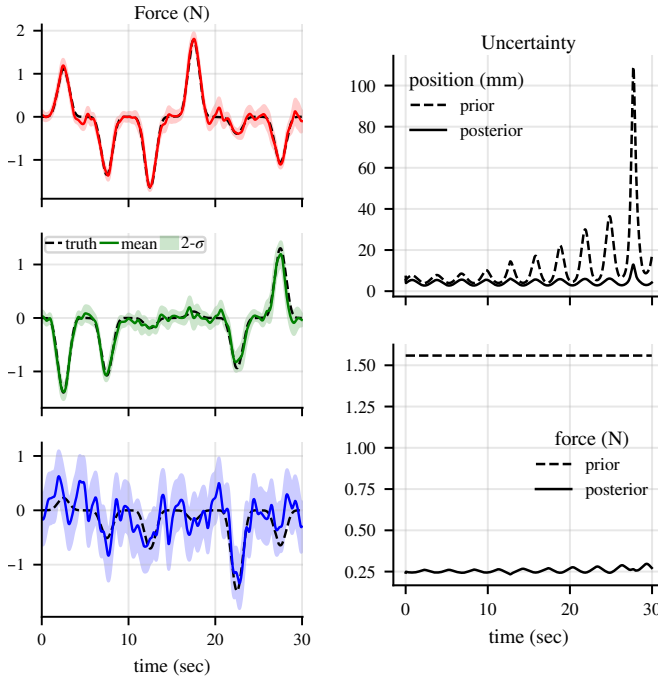


**Fig. 8:** Parallel robot simulation results (24.02 ms mean solve time over 900 time steps). *Left:* Estimated tip force over the trajectory. *Right:* Overall position and force uncertainty  $\sqrt{\text{Tr}(\Sigma)}$  throughout the trajectory.

## V. PARALLEL CONTINUUM ROBOTS

Given the base Cosserat rod graph (Figure 2), we can very naturally connect multiple rods together to form closed loop topologies, allowing us to model parallel continuum robots within our framework (Figure 7). One way to do this is by constraining the tips of multiple rods with respect to a shared platform. Here we present a factor graph representation for the platform robot in [17]; constraining rods to each other [5] is a straightforward extension. The approach is similar to [8], except that we also model applied forces on the rods.

Instead of enforcing constraints with a BVP outer solve [17], we place platform constraint factors and solve all of the

rods in batch. For the rigid platform constraints, we include known geometry factors between each of the rod tips  $\mathbf{T}_{K,i}$  and the platform pose  $\mathbf{T}_p$  (yellow factors in Figure 7):

$$\left\| \log\text{map} \left( \bar{\mathbf{T}}_{p,i}^{-1} \mathbf{T}_p^{-1} \mathbf{T}_{K,i} \right) \right\|_{\Sigma_{T_p}}, \quad (24)$$

where  $\bar{\mathbf{T}}_{p,i}$  is the tip offset of rod  $i$ . Partial pose constraints [5] can also be modeled by changing the components of  $\Sigma_{T_p}$ .

To enforce the overall wrench balance between the rods and the platform, we again use the adjoint wrench transport on each rod tip and sum to zero at  $\mathbf{T}_p$  (orange factor in Figure 7):

$$\left\| \sum_i \text{Ad}^T(\mathbf{T}_{K,i}^{-1} \mathbf{T}_p) \mathbf{S}_{K,i} - \text{Rot}^T(\mathbf{T}_p) \mathbf{F}_p \right\|_{\Sigma_{F_p}} \quad (25)$$

Finally, to incorporate noisy actuator measurements, we place vertical displacement measurement factors the base of each rod:

$$\left( [0 \ 0 \ 1] \text{Pos}(\mathbf{T}_{0,i}) - \mathbf{q}_i \right)^2 / \sigma_q^2. \quad (26)$$

We optimize the overall parallel robot factor in Figure 7, in a similar way as before in Section III-D.

### A. Tip Force Sensing Simulations

Interaction forces applied to the platform can be inferred from the actuator efforts at the base of each rod [17]. In our simulations, this is done by simulating the base vertical reaction forces with a separate model and injecting noise. For inference, the measurements are incorporated via a simple prior wrench factor at each rod base:

$$\left( [0 \ 0 \ 0 \ 0 \ 0 \ 1] \mathbf{F}_{0,i} - \mathbf{z}_i \right)^2 / \sigma_z^2. \quad (27)$$

We again first test the numerical integration accuracy without any measurements a deterministic BVP solver similar to [17] with 0.06% rod length tip position error, indicating excellent open loop accuracy without any measurements.

For state estimation including observations, we use the same simulation approach from Section IV-C, again using 23 to extract the Jacobian to track a spiral-shaped goal trajectory, that spirals out over time. A qualitative examples of the posterior can be seen at a single time step in Figure 7 (right) and detailed results in Figure 8. We again see force estimation that is consistent with the ground truth. We also see that including measurements of actuator *forces* significantly improved *position* uncertainty (Figure 8, right), likely due to the coupling between wrenches and shape.

## VI. CONCENTRIC TUBE ROBOT EXPERIMENTS

Finally, we apply our framework to a real-world surgical concentric tube robot (Figure 9). An arm of the Virtuoso system is comprised of two telescoping tubes which are actuated by independently rotating and translating at their bases. However, the long endoscope channel can induce torsion/backlash, leading to significant actuation uncertainty.

Since the inner tube is straight, we model the (left) arm relatively simply by attaching two Cosserat rod graphs (see

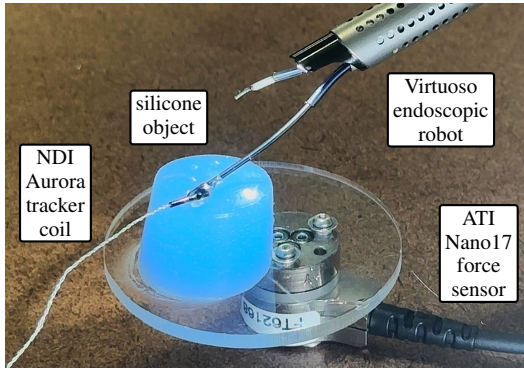


**Fig. 9:** Surgical concentric tube robot experiment setup. The robot was teleoperated to touch a silicone object several times, simulating soft tissue palpation. The object was attached to a force/torque sensor to measure interaction forces, and a magnetic tracking coil was attached to the tip of the robot to measure tip pose.

Figure 2) in series. The outer tube is given a prior pose (14) based on its rotation, and insertion actuation is enforced by an appropriate  $\Delta s$ . The inner tube is set similarly by connecting its base pose to the outer tube tip pose. Actuation uncertainty is incorporated by setting the covariance on these base poses.

We use ROS2 to record all data streams from the the tracker, force sensor, and the robot. We collected an initial data set without the robot to calibrate the force sensor rotation to the tracker. Next, we collected a calibration data set to calibrate the overall setup, teleoperating the robot to move around its workspace while palpating the blue silicone object, imparting contact forces. Using this data, we performed a joint maximum likelihood optimization to estimate: tracker pose, tube curvatures, tube bending/torsion stiffness, and all actuation noise parameters. We collected a second data set for evaluation of two operating modes. Example snapshots are shown in Figure 1, and detailed results in Figure 10.

All of the measured values typically lie within the uncertainty envelopes, indicating good calibration. Given known tip force, the forward model was able to accurately estimate shape. The inverse force sensing application was also reasonably accurate. However, tip force sensing is ill-conditioned in the axial  $z$  direction, likely due to high stiffness compared with tracker noise. Indeed, the estimated  $z$  force was nearly identical to the prior, indicating a lack of information. Therefore, additional information should be used for fully accurate 3D force sensing.

## VII. CONCLUSION

We presented a framework for continuum robot state estimation that models actuation uncertainty. Our discrete Cosserat rod formulation achieves high integration accuracy and enables straightforward, sparse optimization. We demonstrated the approach in simulation on tendon-driven and parallel continuum robots, validating against standard baselines, and showed how manipulator Jacobians can be immediately extracted from the graph. Experiments on a surgical concentric tube robot further confirmed accurate estimation, highlighting applications in tissue palpation. Overall,

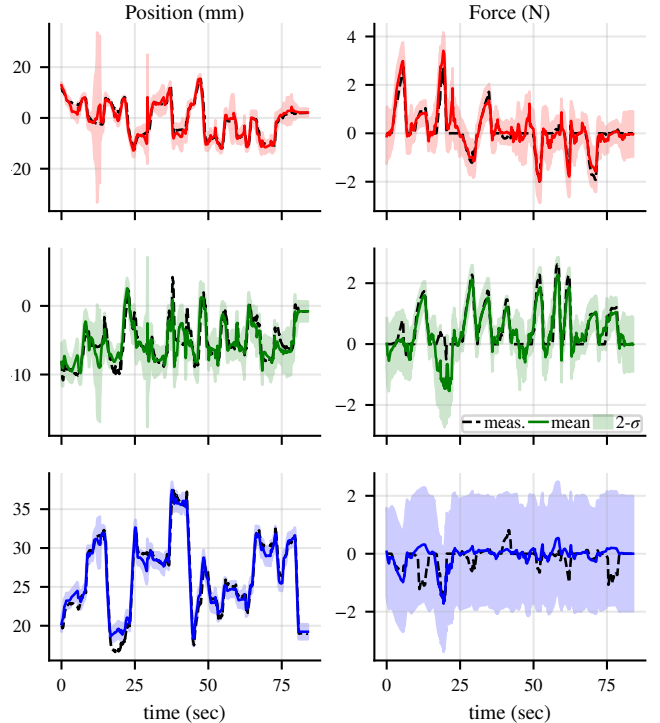


**Fig. 10:** Experimental concentric tube robot results *Left:* Forward model predicting shape given measured actuation and tip forces (**2.41 ms** mean solve time over 900 time steps). Mean tip position accuracy relative to the tracker was **1.95 mm**. *Right:* Inverse model predicting loads given measured actuation and tip position (**2.58 ms** mean solve time). Mean tip force accuracy relative to the sensor was **0.49 N**. mean force error).

our results demonstrate a principled, real-time solution for continuum robot estimation across diverse actuation models.

Future work includes extending the framework with temporal space–time factors [32] for smoothing, incorporating inertial and finite-difference factors for rod dynamics, and integrating additional sensing modalities (e.g., endoscope cameras) or robot models (e.g., torsionally interacting tubes).

## APPENDIX I LINEARIZED ERROR TERMS

Here we show linear approximations of our key error models, which enable accurate and efficient optimization steps. Looking at (8), the kinematics error  $e_{T_k}$  is nonlinear only in the pose variables, which we perturb on the right; e.g.  $\mathbf{T}_k = \bar{\mathbf{T}}_k \exp(\hat{\boldsymbol{\xi}}_k)$ . Defining  $\bar{\Delta} = \bar{\mathbf{T}}_k^{-1} \bar{\mathbf{T}}_{k+1}$  it is straightforward to show (Baker–Campbell–Hausdorff [3]),

$$\begin{aligned} \ln(\mathbf{T}_k^{-1} \mathbf{T}_{k+1})^\vee &= \ln(\exp(-\hat{\boldsymbol{\xi}}_k) \bar{\Delta} \exp(\hat{\boldsymbol{\xi}}_{k+1}))^\vee \approx \\ &\ln(\bar{\Delta}) - \mathbf{J}_r^{-1}(\bar{\Delta}) \text{Ad}(\bar{\Delta}) \hat{\boldsymbol{\xi}}_k + \mathbf{J}_r^{-1}(\bar{\Delta}) \hat{\boldsymbol{\xi}}_{k+1}, \end{aligned} \quad (28)$$

where  $\mathbf{J}_r$  is the right Jacobian of  $\text{SE}(3)$ .

The mechanics error  $e_{S_k}$  is again only nonlinear in the pose variables. For the first term in (12), we start by linearizing with respect to the intermediate variable  $\Delta = \mathbf{T}_k^{-1} \mathbf{T}_{k+1} = \bar{\Delta} \exp(\hat{\boldsymbol{\delta}}^\wedge)$ :

$$\begin{aligned} \text{Ad}^T(\bar{\Delta} \exp(\hat{\boldsymbol{\delta}}^\wedge)) \mathbf{S}_k &\approx (\mathbf{I} + \text{ad}^T(\hat{\boldsymbol{\delta}})) \text{Ad}^T(\bar{\Delta}) \mathbf{S}_k \\ &= \text{Ad}^T(\bar{\Delta}) \mathbf{S}_k + \text{ad}^T(\hat{\boldsymbol{\delta}}) \text{Ad}^T(\bar{\Delta}) \mathbf{S}_k. \end{aligned} \quad (29)$$

Letting  $\text{Ad}^T(\bar{\Delta})\mathbf{S}_k = (\omega, v)$ , and  $\delta = (\delta_\omega, \delta_v)$  we rewrite the second term in (29) as

$$\begin{bmatrix} \delta_\omega^\wedge & 0 \\ \delta_v^\wedge & \delta_\omega^\wedge \end{bmatrix}^T \begin{bmatrix} \omega \\ v \end{bmatrix} = \begin{bmatrix} \omega^\wedge & v^\wedge \\ v^\wedge & 0 \end{bmatrix} \begin{bmatrix} \delta_\omega \\ \delta_v \end{bmatrix} = \mathcal{A}\delta. \quad (30)$$

Using this and the SE(3) perturbation linearization  $\delta = -\text{Ad}(\bar{\Delta})\xi_k + \xi_{k+1}$ , the overall linearization is

$$\begin{aligned} & \text{Ad}^T(\mathbf{T}_k^{-1}\mathbf{T}_{k+1})\mathbf{S}_k \\ & \approx \text{Ad}^T(\bar{\Delta})\mathbf{S}_k - \mathcal{A}\text{Ad}(\bar{\Delta})\xi_k + \mathcal{A}\xi_{k+1}. \end{aligned} \quad (31)$$

Linearizing the second term in (12) with respect to  $\mathbf{T}_{k+1}$  is straightforward using the SO(3) perturbation approximation

$$Rv = \bar{R}\exp(\delta r^\wedge)v \approx \bar{R}v - \bar{R}v^\wedge\delta r. \quad (32)$$

The derivatives of  $\mathbf{e}_{D_d}$  in (21) are computed with a large sum/product/chain rule, via linearizing (20) with respect to the poses. The other derivatives are either simple or straightforward extensions (e.g. (25) is very similar to (12)). All computation details can be found in our source code.

## REFERENCES

- [1] J. Burgner-Kahrs, D. C. Rucker, and H. Choset, "Continuum robots for medical applications: A survey," *IEEE Transactions on Robotics*, vol. 31, no. 6, pp. 1261–1280, 2015.
- [2] M. Russo, S. M. H. Sadati, X. Dong, A. Mohammad, I. D. Walker, C. Bergeles, K. Xu, and D. A. Axinte, "Continuum robots: An overview," *Advanced Intelligent Systems*, vol. 5, no. 5, 2023.
- [3] T. D. Barfoot, *State estimation for robotics*. Cambridge University Press, 2017.
- [4] F. Dellaert, "Factor graphs: Exploiting structure in robotics," *Annual Review of Control, Robotics, and Autonomous Systems*, vol. 4, no. 1, pp. 141–166, 2021.
- [5] P. L. Anderson, A. W. Mahoney, and R. J. Webster, "Continuum reconfigurable parallel robots for surgery: Shape sensing and state estimation with uncertainty," *IEEE robotics and automation letters*, vol. 2, no. 3, pp. 1617–1624, 2017.
- [6] J. M. Ferguson, D. C. Rucker, and R. J. Webster, "Unified shape and external load state estimation for continuum robots," *IEEE Transactions on Robotics*, vol. 40, pp. 1813–1827, 2024.
- [7] S. Lilge, T. D. Barfoot, and J. Burgner-Kahrs, "Continuum robot state estimation using gaussian process regression on se (3)," *The International Journal of Robotics Research*, vol. 41, no. 13-14, pp. 1099–1120, 2022.
- [8] —, "State estimation for continuum multi-robot systems on se (3)," *IEEE Transactions on Robotics*, 2024.
- [9] S. Lilge and T. D. Barfoot, "Incorporating control inputs in continuous-time gaussian process state estimation for robotics," *Robotica*, vol. 43, no. 3, pp. 1067–1086, 2025.
- [10] D. B. Camarillo, K. E. Loewke, C. R. Carlson, and J. K. Salisbury, "Vision based 3-d shape sensing of flexible manipulators," in *IEEE International Conference on Robotics and Automation*, 2008, pp. 2940–2947.
- [11] M. W. Hannan and I. D. Walker, "Real-time shape estimation for continuum robots using vision," *Robotica*, vol. 23, no. 5, pp. 645–651, 2005.
- [12] B. Kim, J. Ha, F. C. Park, and P. E. Dupont, "Optimizing curvature sensor placement for fast, accurate shape sensing of continuum robots," in *IEEE international conference on robotics and automation*, 2014, pp. 5374–5379.
- [13] V. Modes, T. Ortmaier, and J. Burgner-Kahrs, "Shape sensing based on longitudinal strain measurements considering elongation, bending, and twisting," *IEEE Sensors Journal*, vol. 21, no. 5, pp. 6712–6723, 2020.
- [14] S. C. Ryu and P. E. Dupont, "Fbg-based shape sensing tubes for continuum robots," in *IEEE International Conference on Robotics and Automation*, 2014, pp. 3531–3537.
- [15] Q. Zhao, J. Lai, K. Huang, X. Hu, and H. K. Chu, "Shape estimation and control of a soft continuum robot under external payloads," *IEEE/ASME Transactions on Mechatronics*, vol. 27, no. 5, pp. 2511–2522, 2021.
- [16] A. Kuntz, A. Sethi, R. J. Webster, and R. Alterovitz, "Learning the complete shape of concentric tube robots," *IEEE transactions on medical robotics and bionics*, vol. 2, no. 2, pp. 140–147, 2020.
- [17] C. B. Black, J. Till, and D. C. Rucker, "Parallel continuum robots: Modeling, analysis, and actuation-based force sensing," *IEEE Transactions on Robotics*, vol. 34, no. 1, pp. 29–47, 2017.
- [18] V. Aloï, K. T. Dang, E. J. Barth, and C. Rucker, "Estimating forces along continuum robots," *IEEE Robotics and Automation Letters*, vol. 7, no. 4, pp. 8877–8884, 2022.
- [19] D. C. Rucker and R. J. Webster, "Deflection-based force sensing for continuum robots: A probabilistic approach," in *IEEE/RSJ International Conference on Intelligent Robots and Systems*, 2011, pp. 3764–3769.
- [20] A. Brij Koolwal, F. Barbagli, C. Carlson, and D. Liang, "An ultrasound-based localization algorithm for catheter ablation guidance in the left atrium," *The International Journal of Robotics Research*, vol. 29, no. 6, pp. 643–665, 2010.
- [21] J. A. Borgstadt, M. R. Zinn, and N. J. Ferrier, "Multi-modal localization algorithm for catheter interventions," in *IEEE international conference on robotics and automation*, 2015, pp. 5350–5357.
- [22] Q. Qiao, G. Borghesan, J. De Schutter, and E. Vander Poorten, "Force from shape—estimating the location and magnitude of the external force on flexible instruments," *IEEE Transactions on Robotics*, vol. 37, no. 5, pp. 1826–1833, 2021.
- [23] D. C. Rucker and R. J. Webster III, "Statics and dynamics of continuum robots with general tendon routing and external loading," *IEEE Transactions on Robotics*, vol. 27, no. 6, pp. 1033–1044, 2011.
- [24] O. Weeger, S.-K. Yeung, and M. L. Dunn, "Isogeometric collocation methods for cosserat rods and rod structures," *Computer Methods in Applied Mechanics and Engineering*, vol. 316, pp. 100–122, 2017.
- [25] A. L. Orekhov and N. Simaan, "Solving cosserat rod models via collocation and the magnus expansion," in *IEEE/RSJ International Conference on Intelligent Robots and Systems*, 2020, pp. 8653–8660.
- [26] S. H. Sadati, S. E. Naghibi, I. D. Walker, K. Althoefer, and T. Nanayakkara, "Control space reduction and real-time accurate modeling of continuum manipulators using ritz and ritz–galerkin methods," *IEEE Robotics and Automation Letters*, vol. 3, no. 1, pp. 328–335, 2017.
- [27] S. Grazioso, G. Di Gironimo, and B. Siciliano, "A geometrically exact model for soft continuum robots: The finite element deformation space formulation," *Soft robotics*, vol. 6, no. 6, pp. 790–811, 2019.
- [28] M. Xie and F. Dellaert, "A unified method for solving inverse, forward, and hybrid manipulator dynamics using factor graphs," *arXiv preprint arXiv:1911.10065*, 2019.
- [29] M. Xie, A. Escontrela, and F. Dellaert, "A factor-graph approach for optimization problems with dynamics constraints," *arXiv preprint arXiv:2011.06194*, 2020.
- [30] J.-L. Blanco-Claraco, A. Leanza, and G. Reina, "A general framework for modeling and dynamic simulation of multibody systems using factor graphs," *Nonlinear Dynamics*, vol. 105, no. 3, pp. 2031–2053, 2021.
- [31] J. Dong, M. Mukadam, F. Dellaert, and B. Boots, "Motion planning as probabilistic inference using gaussian processes and factor graphs," in *Robotics: Science and Systems*, vol. 12, no. 4, 2016, pp. 10–15 607.
- [32] S. Teetaert, S. Lilge, J. Burgner-Kahrs, and T. D. Barfoot, "A stochastic framework for continuous-time state estimation of continuum robots," *arXiv preprint arXiv:2510.01381*, 2025.
- [33] F. Renda, F. Boyer, J. Dias, and L. Seneviratne, "Discrete cosserat approach for multisection soft manipulator dynamics," *IEEE Transactions on Robotics*, vol. 34, no. 6, pp. 1518–1533, 2018.
- [34] A. Gao, Y. Zou, Z. Wang, and H. Liu, "A general friction model of discrete interactions for tendon actuated dexterous manipulators," *Journal of Mechanisms and Robotics*, vol. 9, no. 4, p. 041019, 2017.
- [35] D. C. Rucker and R. J. Webster, "Computing jacobians and compliance matrices for externally loaded continuum robots," in *2011 IEEE international conference on robotics and automation*. IEEE, 2011, pp. 945–950.